# Selectivity and competition between the anodic evolution of oxygen and chlorine

Vos, J.G.

# 5

# COMPETITION AND SELECTIVITY DURING PARALLEL EVOLUTION OF BROMINE, CHLORINE AND OXYGEN ON $IrO_x$ ELECTRODES

Oxidation reactions related to bromide have a very low thermodynamic threshold relative to the OER and CER, and present a substantial problem in electrolyzers where seawater is the desired feedstock. In this chapter we continue the work and analysis methods used in Chapter 4 in order to understand parallel evolution of bromine and chlorine on Pt, and extend it to $IrO_x$, focusing on the OER and how it is affected in the presence of chloride and bromide. Chloride and bromide absorb competitively on $IrO_x$, but contrary to Pt, we found no evidence of interhalogen BrCl formation. We also found that even a relatively small amount of bromide strongly slows down both the CER and OER, where especially the OER and its selectivity is highly affected. This knowledge can lead to a deeper understanding of the challenges to be faced when developing an OER-selective anode for seawater electrolysis.

THIS CHAPTER IS BASED ON THE FOLLOWING

**PUBLICATION:**

Vos, J. G.; Venugopal, A.; Smith, W.A.; Koper, M. T. M. Competition and Selectivity During Parallel Evolution of Bromine, Chlorine and Oxygen on IrOx Electrodes. Manuscript in preparation (2019).

## 5.1. Introduction

In Chapter 4, we explored the parallel oxidation of chloride and bromide on Pt within the context of seawater electrolysis, which would involve electrolytes that contain both $Cl^-$ and $Br^-$ salts. On Pt, we observed competitive effects and the likely formation of the interhalogen BrCl during halogen evolution. In this chapter, we extend this work to the previously studied amorphous $IrO_x$ catalyst, which is OER-capable and representative for typical metal oxides used in neutral and acid PEM electrolyzers. The OER is the sole desired anodic reaction in such an electrolyzer; the oxidation of either $Cl^-$ or $Br^-$ leads to toxic side-products that undermine the environmentally friendly potential of the electrolysis process, and should therefore ultimately be avoided. Having studied the effect of parallel CER on the OER in Chapters 2 and 3, we hope to aid progress towards an OER-selective anode in seawater by now including the effect of the parallel CER and BER (Eq. 4.1) on the evolution of oxygen.

The BER is generally ignored in the context of seawater electrolysis, because the bromide concentration in seawater is relatively low (0.3%mol relative to the chloride concentration).[186] However, its standard potential is notably lower than that of the CER and OER. Bromide oxidation can thus easily occur in an electrolyzer, especially since like the CER, the overpotential of the BER can be vanishingly small. Additionally, scaling behavior between the OER and CER has been reported in previous literature and Chapter 3 of this thesis (see also section 1.3). As the BER and CER appear to have very similar reaction mechanisms on a variety of surfaces,[118,196–198] it is expected that a similar scaling exists between the BER and the OER. Both the CER and BER are thus serious competitors to the sluggish OER, which is associated with a significant overpotential.

Despite its particular relevance to seawater electrolysis, the simultaneous evolution of $Br_2$, $Cl_2$ and $O_2$ has been little explored.[193–195] Furthermore, very little is known of the BER mechanism on a metal oxide catalyst, and how it may influence the concurrent CER and OER. $Br^-$ likely competes for adsorption on the same active sites on the catalyst, which would slow down the other two reactions. As was observed during the parallel CER and BER on Pt in Chapter 4, adsorbed reactive Br and Cl species could also lead to formation of interhalogen compounds, such as BrCl, making the system more unpredictable. By simultaneously studying the BER, CER and OER, and looking deeper into their competitive behavior, it is intended to expand knowledge on these issues and also broaden the general understanding of the individual reaction mechanisms.

In this chapter, the parallel evolution of $Br_2$ and $Cl_2$ during $O_2$ evolution is studied in acidic media ($pH \approx 0.35$), where they can be studied with minimum interference from reactions that lead to oxygenated halogen species, such as $BrO_3^-$ or $ClO^-$.[201,202,210] The previously studied GC-supported $IrO_x$ was taken as anodic electrocatalyst. Heavy use will be made of the RRDE technique described in Chapter 2, where the Pt ring served as a detector for $Cl_2$ evolved. This technique will be extended and appended with modelling to separate the individual BER, CER and OER related activities. The $IrO_x$ electrocatalyst could also be conveniently electrodeposited as optically transparent thin layers, once more allowing the analysis of the

identities of halogen oxidation products near stationary electrode surfaces, using online transmission UV-Vis experiments.

## 5.2. Experimental

All experiments were carried out at room temperature (~20 °C). RRDE experiments are inherently more susceptible to contamination than stationary UV-Vis experiments. Cleaning preparations for forced convection experiments were therefore significantly more elaborate.

### *5.2.1. Chemicals*

For the RRDE experiments, $HClO_4$ (70%, Suprapur®/Trace analysis grade) $KHSO_4$ (EMSURE/Analysis grade), KCl (EMSURE/Analysis grade) and HCl (30%, Ultrapur®/Trace analysis grade) were purchased from Merck. HBr (47%, Normapur®/Analysis grade) was purchased from VWR Chemicals. For the UV-Vis experiments, $HClO_4$ (60%, EMSURE/Analysis grade), HCl (32%, EMSURE/Analysis grade) and HBr (47%, EMSURE/Analysis grade) were purchased from Merck. $Na_2IrCl_6 \cdot 6H_2O$ (99.9%, trace metals basis) and NaOH (30% solution, TraceSelect) were purchased from Sigma-Aldrich. All purchased chemicals were used as received. The water used for all experiments was prepared by a Merck Millipore Milli-Q system (resistivity 18.2 MΩcm, TOC < 5 p.p.b.).

### *5.2.2. Cleaning procedures*

All glassware in the RRDE experiments was boiled in a 3:1 mixture of concentrated $H_2SO_4$ and $HNO_3$ before first-time use. When not in use, all glassware was stored in a 0.5 M $H_2SO_4$ solution containing 1 g/L $KMnO_4$. Before each RRDE experiment, all glassware was first rinsed with water, and then submerged in a dilute (~0.01 M) solution of $H_2SO_4$ and $H_2O_2$ to remove all traces of $KMnO_4$ and $MnO_2$. It was then rinsed three times with water and boiled in water. The final rinsing-boiling procedure was repeated two more times.

The glassware and custom-built PTFE cell for UV-Vis experiments were cleaned by soaking in warm reagent grade 98% $H_2SO_4$ for an hour, followed by thorough rinsing with Milli-Q water and boiling three times in Milli-Q water. When not in use, they were stored submerged in Milli-Q water.

### *5.2.3. Electrode preparation*

#### *5.2.3.1. RRDE experiments*

$IrO_x$/GC electrodes were prepared via electroflocculation of $IrO_x$ nanoparticles, as described in sections 9.1.1 and 9.1.2. Diamond paste was used for GC polishing, and the electrode was then rinsed and sonicated in water for 3 minutes. A time duration of 300 s was used for the electroflocculation amperometry step.

Before each experiment, the $IrO_x$ surface was subjected to a pre-treatment step to ensure reproducible activity (see Figure A 9.5.2). The electrode was first kept at 0 V vs. RHE for 10 s,

followed by a 3 s hold at 0.9 V, in order to equilibrate the electrode and allow pseudocapacitive charging to decay to a minimum. Scanning commenced immediately afterwards. The Pt ring electrode was electropolished before experiments by scanning from -0.1 V to 1.7 V at 500 mV $s^{-1}$ for 20 scans at 1500 RPM, followed by removal of gas bubbles adhered to the tip (see also Chapter 8). Ring currents were corrected for constant background currents and product collection delay. The latter arises from the time needed for products formed on the disk to reach the ring and was empirically determined for each investigated rotation rate.

*5.2.3.2. UV-Vis experiments*

Conductive fluorine doped tin oxide (FTO) substrates (TEC-15) were purchased from Hartford glass co. The FTO substrates were cleaned by sonication, using a sequence of laboratory soap, Milli-Q water, acetone, isopropanol and water, followed by drying the substrates with compressed air. $IrO_x$ deposition was then performed using the same prepared colloid solutions and voltammetry-amperometry protocol described in section 5.2.3.1. The FTO substrates were placed upright in the solution, with a LowProfile Ag/AgCl reference electrode aligned to the center of the electroactive surface and a circular Pt counter electrode placed symmetrically around the bottom. Instead of a rotating tip, a stirrer bar at the bottom of the cell rotating at ~400 RPM was used to induce mass flow of the $IrO_x$ particles during deposition.

*5.2.4. Cell preparation*

*5.2.4.1. RRDE experiments*

An IviumStat potentiostat (Ivium Technologies) with IviumSoft software was used in all experiments for potential control. The electrode assemblies were E6 ChangeDisk RRDE tips with a PEEK shroud, attached to an MSR rotator (Pine Research). All experiments were 95% iR-compensated in-situ, by measuring the solution resistance with electrochemical impedance spectroscopy at 0.90 V vs. RHE on the disk, and observing the absolute impedance in the high frequency domain (100-50 KHz) corresponding to a zero-degree phase angle. All used solutions were saturated and continuously bubbled with Ar gas (Linde, purity 6.0) during experiments. The reference electrode was a HydroFlex® reversible hydrogen electrode (Gaskatel), separated from the main solution using a Luggin capillary, with the capillary tip purposely aligned to the center of the working electrode.[231] An additional LowProfile Ag/AgCl reference electrode served to measure the solution pH and was used for interconversion between the NHE and RHE scale. The Ag/AgCl reference was externally calibrated on a regular basis and had a value of 199 ± 0.5 mV vs. NHE. A Pt mesh was used as counter electrode, separated from the main solution by a coarse sintered glass frit.

*5.2.4.2. UV-Vis experiments*

A Vertex potentiostat (Ivium Technologies) run by the IviumSoft software package was used for potential control. Transmission measurements were performed in a custom-built setup, consisting of a PTFE electrochemical cell housing equipped with quartz windows. A coiled platinum wire was used as the counter electrode, and a LowProfile Ag/AgCl reference

electrode (Pine Research) was placed in fixed position relative to the $IrO_x$/FTO working electrode. The Ag/AgCl electrode was calibrated at 199 ± 1 mV vs. NHE. All applied potentials were 90% iR-compensated according to the solution resistance, which was measured using a similar procedure as in section 5.2.4.1. To achieve a wide spectrum in the incoming beam, a deuterium lamp (Mikropack D-2000) and a halogen lamp (Ocean Optics HL 2000 – FHSA), were used in the setup. These light sources were combined using an optical fiber arrangement and this fiber acted as the illumination source for the transmission measurements. A Maya 2000 Pro spectrometer (Ocean Optics) was used to capture the transmitted light. The setup was aligned in such a way that the $IrO_x$/FTO samples were illuminated from the back side and the transmitted light was captured on the opposite side of the electrochemical cell. The transmission data was recorded simultaneously with the electrochemical measurements.

## 5.3. Results and discussion

### *5.3.1. Brief review of the BER and CER kinetics on metal oxides*

Similar to Chapter 4, we will again look closely at experimentally determined Tafel slopes ($b$) and reaction orders ($\mathcal{R}$) to better understand the underlying halogen oxidation mechanisms (see section 1.4). The Langmuir isotherm assumed in the models is likely an oversimplification, but the use of a more complex isotherm, such as devised by Frumkin, does not change the previously described limits for $b$ and $\mathcal{R}$ when either $\theta \to 0$ or $\theta \to 1$. Their shape and width as function of $E$ and $[Cl^-]$ will however depend sensitively on the isotherm. The discussion of experimental findings will be restricted to some general trends and possible limiting values.

In previous literature, the mechanism of the CER on metal oxides has been studied extensively, but despite this it still has some uncertainty. The main issue is that combined $\mathcal{R}_{Cl^-}$ values and Tafel slopes often do not satisfactorily agree with predictions of either the Volmer-Heyrovský (V-H) or Volmer-Krishtalik (V-K) mechanisms. As can be seen from Eq. 1.12, the driving force for $Cl^-$ adsorption depends on both the potential $E$ and the bulk chloride concentration. As $\theta_{Cl}$ changes from 0 to 1 under the effect of increasing $\eta$ and/or $[Cl^-]$, the V-H mechanism predicts that the chloride reaction order $\mathcal{R}_{Cl^-}$ decreases from 2 to 1, and that the Tafel slope increases from ~40 mV/dec to ~120 mV/dec (under the assumption that $\alpha_H \approx 0.5$). Tafel slopes of ~40 mV/dec at low overpotentials have indeed often been observed in experiments, pointing to the theoretical limit of $\theta_{Cl} \approx 0$. However, the corresponding experimental values for $\mathcal{R}_{Cl^-}$ were almost universally close to 1, suggesting the limit of $\theta_{Cl} \approx 1$.[35,55,110,112,183,184,232] Often, they were also practically invariant versus $E$ and $[Cl^-]$. The V-K mechanism was in fact specifically invoked to account for this problem, as it predicts that $0 \leq \mathcal{R}_{Cl^-} \leq 1$, which is slightly more in-line with these results. Conway and Tilak have postulated that the CER mechanism on metal oxides follows rather the Volmer-Tafel mechanism,[112] but this view is not widely shared. We will discuss our results in adherence with previous literature, although the established discrepancies between the models and experimental results must be kept in mind.

### *5.3.2. Parallel RRDE oxidation currents as function of chloride concentration*

We will first describe our methods and a few general results regarding the parallel BER, CER and OER on the $IrO_x$/GC catalyst. RRDE cyclic voltammetry was used for all kinetic studies, since both the BER and CER are rapid reactions which quickly become diffusion controlled as the overpotential increases. Hydrodynamic conditions keeps the diffusion layer thickness constant in time, simplifying the analysis and allowing a deeper investigation of the role of mass transport. Sufficiently high rotation rates also prevented $Br^-$-related follow-up reactions by removing $Br_2$ formed near the surface. In the spirit of Chapter 2, it was possible to use the RRDE with a Pt ring to selectively reduce halogen species formed in parallel with OER, so that the reactions can be separated and analyzed independently. As in Chapter 4, the ring potential

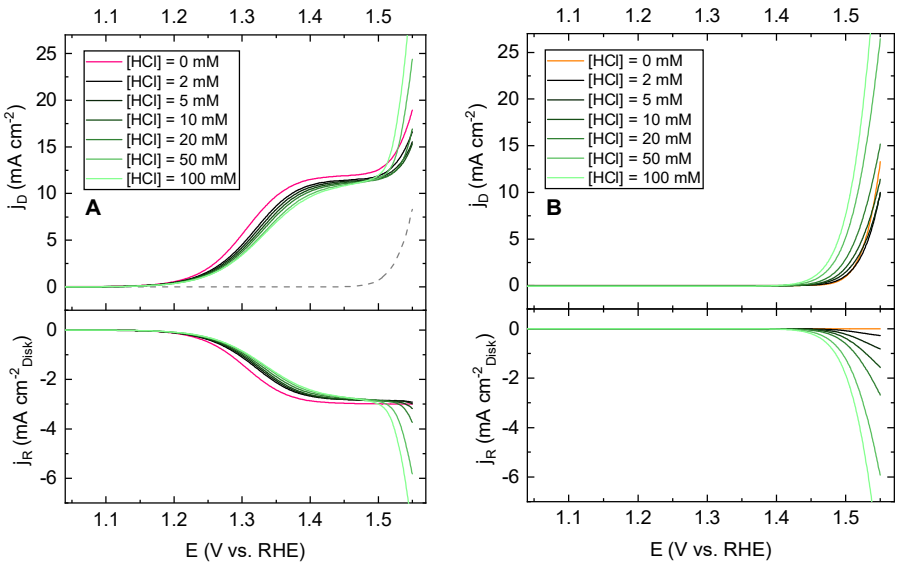


*Figure 5.1: Measured current densities of OER and halogen evolution on an $IrO_x$/GC electrode in 0.5 M $HClO_4$. Top panels show forward, pseudo-capacitance corrected scans of the disk, lower panels show corresponding ring signals measured at 0.7 V vs RHE, corrected for background and collection delay. The effect of increasing HCl concentration is shown from black to green. A: OER in parallel with $Br^-$ and $Cl^-$ oxidation, in presence of 10 mM HBr and 0 – 100 mM HCl. Results in chloride-free conditions (only the BER and OER) are shown in pink. Also shown is the OER activity in absence of both $Br^-$ and $Cl^-$ (grey dotted trace). B: Experiments similar to A, but in $Br^-$-free conditions, with the ring at 0.95 V vs. RHE. Orange trace shows OER activity in absence of $Cl^-$. Solution purged with Ar, rotation rate 1600 RPM, CV's recorded at 50 mV $s^{-1}$.*

was fixed at 0.7 V vs. RHE, where the reduction of oxygen has negligible activity in presence of $Br^-$, and where halogen reduction reactions should thus be fully diffusion limited.

All experimental data were gathered with cyclic voltammograms recorded at 10 mV $s^{-1}$. Forward scans were used for catalytic analysis, while forward and backward scans were used to estimate capacitive currents. These non-catalytic contributions were usually a minor factor (less than 0.1%) in the total current, and were minimized by subtracting a constant value from the forward scan currents. Results were recorded versus the RHE, which is the 'natural' potential scale of the pH-dependent OER. Generally, this scale will be used to report OER-

related results. The studied halogen evolution reactions are however pH-independent. A relatively acidic supporting electrolyte of 0.5 M $HClO_4$ (pH ≈ 0.35) was used to reduce pH changes from the addition of HBr or HCl. Data involving $Br^-$ or $Cl^-$ oxidation are reported versus the NHE scale to account for potential shifts from pH effects, which were very minor (<5 mV).

Figure 5.1A shows some typical results measured on GC-supported $IrO_x$ in a mixed $Br^-$ and $Cl^-$ electrolyte. The onset of bromide oxidation from 10 mM HBr is clearly visible around 1.12 V vs. RHE, and the reaction reaches a plateau near 1.40 V vs. RHE. This plateau stems from diffusion limitations, because its current density is about 95% of the limiting value predicted by the Levich equation. The OER starts around 1.45 V vs. RHE in absence of HBr and HCl (dotted trace in upper panel). In presence of only 10 mM HBr (pink trace in upper panel), the OER appears superimposed on the limiting current of bromide oxidation. A closer inspection shows that its onset is at a slightly higher potential, and the activity is lower than in absence of $Br^-$. As intended, the OER is not captured in the corresponding ring data (lower panel), which only detects the limiting current of bromine evolution. When HCl is added, the ring data show an additional halogen oxidation reaction around 1.45 V vs. RHE, which suggests chloride oxidation starts taking place in parallel with OER. Compared to Figure 5.1B, which shows the parallel evolution of $O_2$ and $Cl_2$ in absence of bromide under otherwise identical conditions, the CER activity is significantly reduced, and has a much higher onset potential. Reciprocally, HCl also imparts some notable changes on the bromide oxidation wave. The bromide oxidation activity is lowered in the whole measured potential range, which becomes more obvious with increasing [$Cl^-$]. Diffusion limitations for bromide oxidation are again apparent around 1.40 V vs. RHE. While bromide and chloride are being oxidized simultaneously, there is no immediate sign of a new onset somewhere in-between the BER and CER, in contrast to results from Figure 4.1C concerning Pt. This suggests that no interhalogen reactions are taking place.

### *5.3.3. Kinetic analysis and reaction orders of bromide oxidation*

The bromide oxidation waves in Figure 5.1 between 1.10 – 1.45 V vs. RHE will be investigated in more detail. For this, Koutecký-Levich plots were constructed by varying the rotation rate (see Figure A 9.5.5 and Figure A 9.5.6) for each combination of [HCl] + 10 mM HBr. The y-intercept of these plots and their closeness to zero can be unambiguously interpreted as a degree of mass transport control over the reaction, especially if the plots are highly linear.

Data in Figure 5.2 was derived from measured disk current densities $j_D$, where up to 1.45 V, no evolution of $Cl_2$ or $O_2$ occurs. In presence of $Cl^-$, formation of the interhalogen BrCl is thermodynamically allowed around potentials >1.19 V vs. NHE (see Table A 9.4.1). We will discuss this issue further below, and for the moment refer to positive currents within 1.10 – 1.40 V vs. NHE in presence of $Cl^-$ as 'bromide oxidation'.

Figure 5.2A shows that the BER (pink trace) is essentially fully diffusion controlled near 1.35 V vs. NHE (~1.38 V vs. RHE). When HCl is present, the intercept values become slightly larger as [$Cl^-$] increases, indicating that the reaction becomes slightly more kinetically controlled

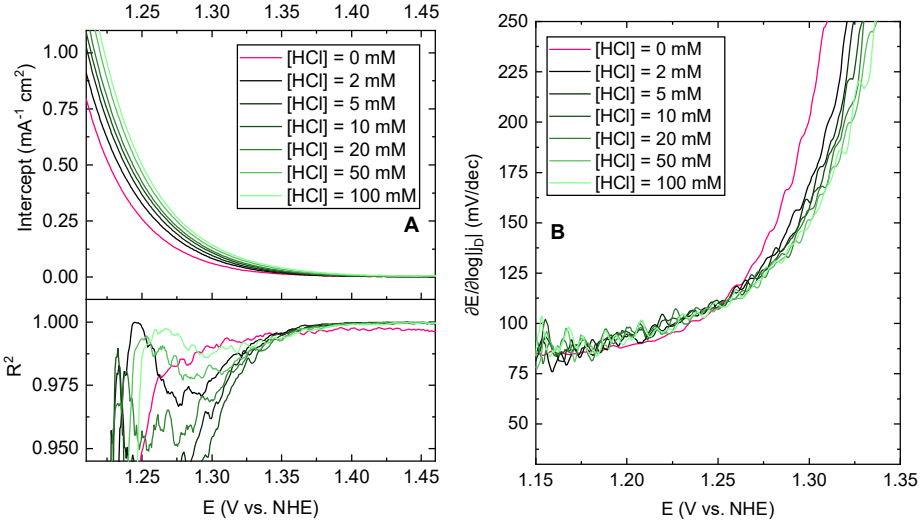


*Figure 5.2: Kinetic data measured in the potential region of bromide oxidation, in 0.5 M $HClO_4$ + 10 mM HBr, for varying concentrations of HCl. Data is shown on the NHE potential scale to account for minor (±4 mV) pH shifts. A: Values of the intercept as function of potential, derived from Koutecký-Levich plots as in Figure A 9.5.6. Pink trace shows data when [HCl] = 0 mM. Top panel shows values of the intercept; lower panel shows corresponding values of the linear correlation coefficient R². B: Tafel slopes obtained from semi-logarithmic data of Figure 5.1 (see Figure A 9.5.11).*

and diffusion limitations are approached more slowly as a function of potential. The reaction nonetheless always becomes diffusion controlled above 1.40 V vs. NHE. In Figure 5.2B, the BER (pink trace) shows a quasi-linear Tafel region between 1.15 – 1.25 V vs. NHE, where values are initially 90 mV/dec and gradually increase with potential. In this region, the effect of HCl is a slight increase of the Tafel slope values. All slopes increase sharply at potentials higher than 1.25 V vs. NHE, which can clearly be ascribed to the onset of mass transport control. The effect of $Cl^-$ is a somewhat more extended potential window of kinetic control.

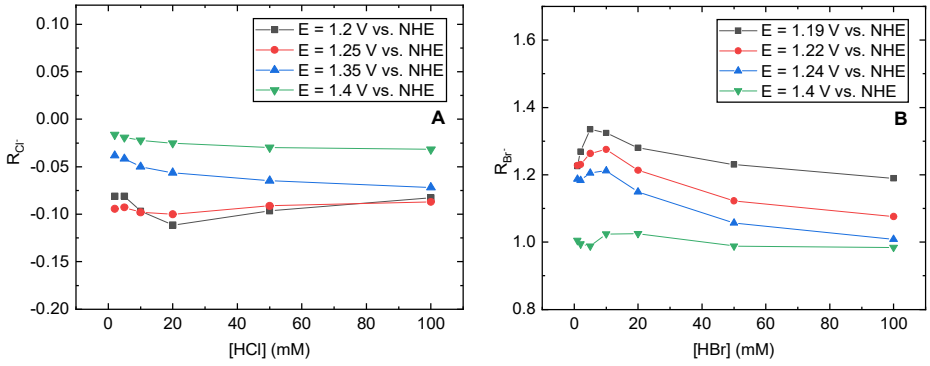


*Figure 5.3: Chloride and bromide reaction orders measured in the potential region of bromide oxidation, in 0.5 M $HClO_4$. Data is shown on the NHE potential scale to account for minor (±4 mV) pH shifts. A: Chloride reaction orders $\mathcal{R}_{Cl^-}$ at several potentials, obtained by varying the HCl concentration at a fixed value [HBr] = 10 mM. B: Bromide reaction orders $\mathcal{R}_{Br^-}$ at several potentials, obtained by varying the HBr concentration in $Cl^-$-free conditions.*

Figure 5.3A shows chloride reaction orders ($\mathcal{R}_{Cl^-}$) for bromide oxidation at a constant [HBr] = 10 mM, derived from log-log plots of current density at constant potential (Figure A 9.5.12). Values for $\mathcal{R}_{Cl^-}$ are slightly negative at all times, as can be visualized by a reduction in bromide oxidation currents by $Cl^-$ in the curves in Figure 5.1A. Observing the quasi-linear Tafel slopes in Figure 5.2B, the reaction is irreversible and kinetically controlled within 1.18-1.25 V vs. NHE; here, $\mathcal{R}_{Cl^-} \approx -0.1$, regardless of potential or chloride concentration. At higher potentials where diffusion limitations dominate, $\mathcal{R}_{Cl^-}$ approaches 0. Furthermore, Figure 5.3B shows bromide reaction orders ($\mathcal{R}_{Br^-}$) for the BER, in absence of $Cl^-$ (see also Figure A 9.5.9). The BER, due to its rather high intrinsic rate, approaches diffusion limitations very quickly. This leads to only a rather narrow potential window of around 1.19 - 1.22 V in which the reaction was kinetically controlled at all measured bromide concentrations. Values of $\mathcal{R}_{Br^-}$ within this window were found to be significantly higher than 1 at low concentrations, and leveled off to lower values as $[Br^-]$ increased. For diffusion-controlled potentials, $\mathcal{R}_{Br^-} \approx 1$, as can be expected when transport of $Br^-$ to the surface is rate-limiting.

The $\mathcal{R}_{Br^-}$ values in Figure 5.3B are best captured by the V-H mechanism, as they are appreciably higher than 1, and (at kinetically controlled potentials) appear to level off to 1 as both $E$ and $[Br^-]$ increase. However, within the Langmuir V-H or V-K formalism, the 'onset value' of ~90 mV/dec for Tafel slopes in Figure 5.2B is quite different from the expected value of ~40 mV/dec at low overpotentials, provided that $\alpha \approx 0.5$. For the BER in a $Cl^-$-free electrolyte, a similar effect was observed (Figure A 9.5.8). Tafel curves in the range of $1\ mM \leq [Br^-] \leq 100\ mM$ had quasi-linear regions, but the slope at the onset of these quasi-linear regions itself depended on the concentration. The most straight-forward interpretation of these results is a coverage effect of $Br^*$. At the onset of the reaction, $\theta_{Br}$ is perhaps significantly high, and the Tafel slope is already changing from 40 to 120 mV/dec. It is also possible that repulsive adsorbate interactions (which are ignored by the Langmuir approximation) play a role. Alternatively, the change in slope may be caused by the formation of higher oxidation states in the $IrO_x$, which starts occurring in the same region where the BER is kinetically controlled. The catalytic capability of $IrO_x$ towards the OER has been shown to sensibly depend on this transition, such that it may also affect intrinsic rates of the BER. In any case, the theoretical upper limit of 120 mV/dec is never observed, possibly because diffusion limitations set in before the required overpotential is reached. To further investigate the bromide oxidation mechanism, we used Conway-Novák and Ferro-de Battisti test plots (Figure A 9.5.10), which offer a method to distinguish between the V-T or V-H mechanisms, respectively. The basis of this method is to rearrange the *j* vs. *E* relationship predicted by those mechanisms (i.e. Eq. 1.14 and Eq. 1.19), to give a straight line. Redrawing the experimental data in the same way and comparing the linearity provides a qualitative indication as to which mechanism the data adhere the best. We found that both Conway-Novák and Ferro-de Battisti plots of the BER data resulted in linearity, but significantly diverged in the high overpotential limit. Current densities in this region increased faster than expected by either mechanism, but Ferro-de Battisti plots gave better linearity overall. Similar results emerged from test plots involving bromide oxidation in presence of $Cl^-$. Like the unusual Tafel slopes, it is possible that transient redox changes in the $IrO_x$ play a role.

When HCl is added, competitive adsorption of $Cl^-$ will take place. The Langmuir V-H and V-K mechanisms predict that, approximately, all Tafel slopes shift horizontally to lower potentials when this happens (see the SI for full details). The change in Tafel slopes in Figure 5.2B versus [HCl] qualitatively agrees with this, but the effect is rather subtle. Additionally it is noted that $\mathcal{R}_{Cl^-}$ for bromide oxidation is always negative. Its value is predicted to be $\mathcal{R}_{Cl^-} = -\theta_{Cl}$ by both the V-H and V-K pathways, where $0 \leq \theta_{Cl} \leq 1$, such that the experimental value of -0.1 can be accommodated. The BER on $IrO_x$ and the effect of $Cl^-$ on this reaction can thus be modelled quite well by the V-H pathway, although describing the competitively adsorbing $Br^*$ and $Cl^*$ adsorbates with the Langmuir isotherm is likely an oversimplification.

We note that parallel adsorbing $Cl^-$ may lead to the formation of interhalogen products. This can be excluded primarily because $Cl^-$ has only a suppressive effect on the activity. If chloride was involved in any reaction, one would intuitively expect an increase in the mass-transport limited current densities of bromide oxidation. Instead, $\mathcal{R}_{Cl^-}$ is close to zero in this region, so that the formation of BrCl, as previously observed on Pt, seems unlikely. Up until roughly 1.40 V vs. NHE, the BER is the only reaction occurring in a mixed $Br^-$ + $Cl^-$ electrolyte.

### *5.3.4. UV-Vis studies of halogen evolution*

At potentials near the onset of the CER and OER, the measured currents become increasingly convoluted. Although the formation of interhalogen compounds, like BrCl, could be excluded up to 1.40 V vs. NHE by kinetic analysis, it becomes difficult to unambiguously assign the disk activity to specific reactions at higher potentials. To reduce this complexity, we investigated the product distribution of halogen species near the surface using electrochemical UV-Vis spectroscopy. We observed the formation of BrCl on Pt in a mixture of $Br^-$ and $Cl^-$ in Chapter 4; of particular interest would be whether a similar phenomenon takes places on $IrO_x$. Interhalogen reactions happening in solution again need to be taken into account, as described in section 4.3.2; we will approach this issue similarly as described in that section and in the discussion of UV-Vis results on Pt. By increasing the potential in 25 mV steps, with a step duration of 30 s, we studied the effect of increasing potential and shifts in solution composition during progressive oxidation reactions for a given constant potential. For the current experiments, a potential range between 1.100 – 1.500 V vs. RHE was chosen (Figure A 9.5.17A). Changes in the total transmission were measured after passing the beam through the back of the $IrO_x$/FTO electrodes and through the electrolyte. These experiments were carried out in 0.1 M $HClO_4$ + 0.1 M HCl, so that pH changes from HBr addition were negligible (on the order of 0.05 unit).

Figure 5.4 shows currents and the complete time-evolution of a typical UV-Vis experiment on an $IrO_x$/FTO electrode during the parallel oxidation of $Br^-$ and $Cl^-$. The currents in Figure 5.4A show the BER onset around 1.20 V vs. RHE, reaching a (diffusion-limited) peak at 1.325 V followed by the onset of a second reaction around 1.425 V vs. RHE. The latter is clearly due to the CER, and appears to be shifted to a ~50 mV higher potential compared to the CER in absence of $Br^-$, similar to results from RRDE experiments. The suppressive effect of $Br^-$ on the chloride oxidation activity is also apparent. As shown in the corresponding UV-Vis spectra

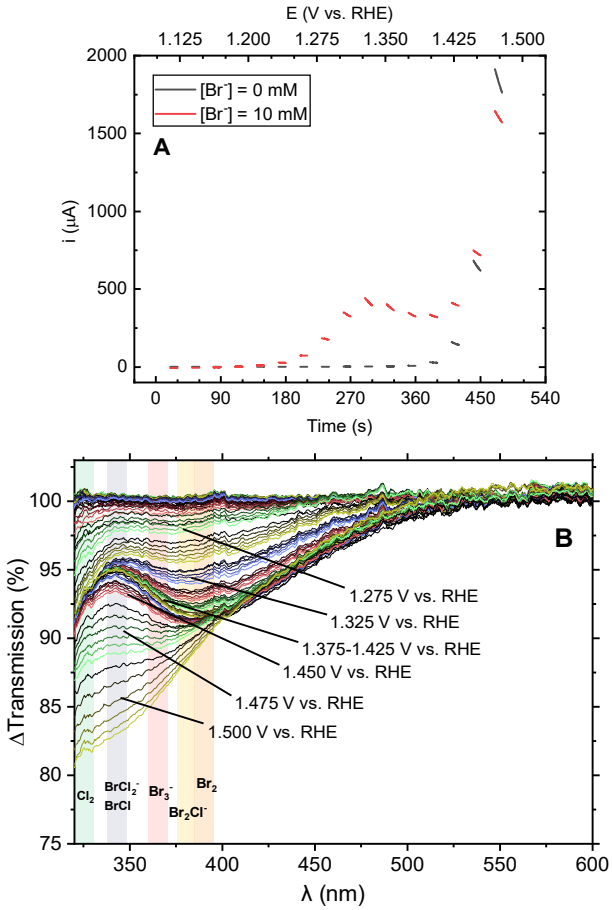


*Figure 5.4: UV-Vis measurements of a stationary $IrO_x$/FTO electrode in a solution of 0.1 M $HClO_4$ + 0.1 M HCl + 10 mM HBr. A: Currents measured during the experiment, where only the final 10 seconds of each potential step are shown for clarity (see Figure A 9.5.17B for full data). Currents in $Br^-$-free conditions are shown for comparison, upper axis shows the potentials applied at each moment in time. B: Corresponding transmission data of the region where the halogen species adsorb. Varying colors among traces correspond to different potential steps, of which some are indicated. Color gradients from dark to light indicate time evolution of the spectra during each potential step.*

in Figure 5.4B, all relevant (inter)halogen species have a secondary adsorption band (or shoulder, in case of $Br_3^-$) that falls in the range 325 – 400 nm. Up until 1.275 V vs. RHE, we observe mild adsorption with a broad shoulder spanning 340 – 450 nm, which suggests that the main species formed is $Br_3^-$.[210] Higher potentials then lead to the sustained growth of a peak around 385 nm, which can be attributed to the formation of $Br_2$ and $Br_2Cl^-$. The currents in Figure 5.4A suggest that bromide oxidation starts to become transport limited around 1.30 V vs. RHE, depleting $Br^-$ near the surface and reversing $Br_3^-$ to $Br_2$ and $Br_2Cl^-$ under the effect of $Cl^-$. This trend then persists over a rather wide potential range, where up until 1.425 V vs. RHE, the only significant change is the growing of the $Br_2$ and $Br_2Cl^-$ signals. $Cl_2$ starts to evolve around 1.450 V vs. RHE, coupled to a sharp decrease in transmission in the wavelengths corresponding to $Cl_2$, BrCl and $BrCl_2^-$. As $Cl_2$ is the most powerful oxidizer in the system under

study, any interhalogen species previously described can now be formed in solution from follow-up reactions with $Br^-$. Crucially, we note that up until 1.425 V vs. RHE, the transmission within 335 – 345 nm is virtually constant, and no shift of the peak around 385 nm to shorter wavelengths is observed. Both observations suggest that BrCl is not formed before the onset of the CER, which was a general finding during experiments with varying concentrations and ratios of $[Br^-]$ and $[Cl^-]$ (see also Figure A 9.5.18 and Figure A 9.5.19). Although the formation of BrCl in parallel with the CER cannot be excluded, it seems reasonable that evolution of $Cl_2$ is the fastest and most prevalent reaction at the high potential limit. In the remainder of this chapter, we will thus assume that the only major electrode reactions are the BER, CER and OER.

### *5.3.5. Kinetic analysis of chlorine and oxygen evolution*

To investigate the CER and OER in the high potential region of Figure 5.1A, the two reactions have to be separated from each other and the underlying BER. We will first describe a method for isolating and modelling these individual currents. As mentioned previously, the ring potential was optimized to selectively reduce halogen evolution products while leaving $O_2$ untouched. The ring response is then proportional to $j_{XER}$, the total halogen evolution current density on the disk, according to (see also Eq. 2.1):

$$j_{XER} = \left|\frac{i_R}{N}\right| \qquad \text{Eq. 5.1}$$

where $j_R$ is the ring current normalized to the disk geometrical surface area (therefore with the same units as $j_D$, mA $cm_{Disk}^{-2}$) and $N$ is the ring-disk collection factor. From the ring currents, it is thus possible to derive $j_{XER}$, which is the sum of the BER and CER current densities, $j_{BER} + j_{CER}$ (Figure A 9.5.3A). Under the reasonable assumption that the $IrO_x$ catalyst is stable, we may then assume that the remainder of $j_D$ after subtraction of $j_{XER}$ is due to OER (see also Eq. 2.2):

$$j_{OER} = j_D - j_{XER} \qquad \text{Eq. 5.2}$$

After calculating $j_{XER}$ from $j_R$, the CER must then be separated from the BER. As in Chapter 4, a strict separation is complex, because the CER and BER are always superimposed, and the underlying contributions of each are not exactly known. However, the bromide oxidation wave generally is fully diffusion controlled at potentials higher than 1.40 V vs. NHE (see section 5.3.2), implying that it follows a sigmoidal trend in the region that is obscured by the onset of chloride oxidation. Like the work concerning Pt (see section 4.3.5), the foot and the top of the bromide oxidation wave were modelled as sigmoidal curves using a 5-parameter generalized logistic function, similar as described in section 4.3.5. Due to competitive adsorption by $Cl^-$ (section 5.3.2), the wave can show notable asymmetry between the foot and the top. This asymmetry was nonetheless captured well by the relatively complex fitting functions (Figure A 9.5.3B). The generalized logistic function at the top of the wave was then used to extrapolate limiting current densities from bromide oxidation near the upper potential limit in $j_{XER}$. The

remaining current density after subtraction can be assigned to the CER. Figure A 9.5.3 shows an example of this procedure.

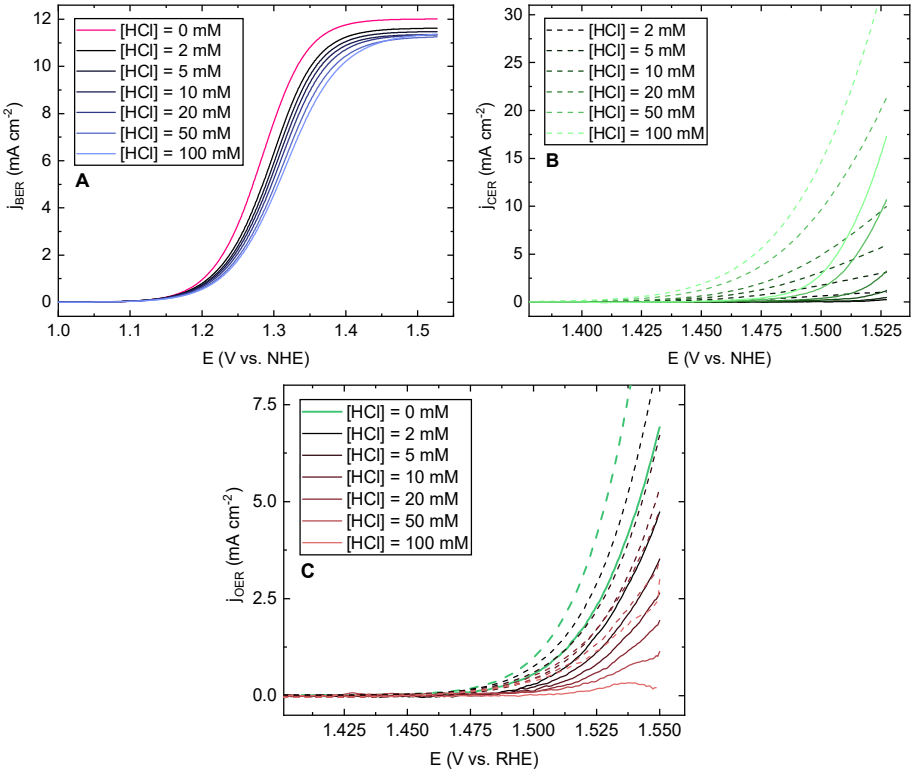


*Figure 5.5: Individual BER, CER and OER current densities during parallel $Br^-$, $Cl^-$ and $H_2O$ oxidation as function of [HCl], on an $IrO_x$/GC electrode in 0.5 M $HClO_4$ and 10 mM HBr. A: BER current densities derived from generalized logistic fits of the foot and top of BER waves in Figure 5.1A. Pink trace shows chloride-free conditions. B and C: CER and OER current densities derived from BER logistic fits and the ring response. Solid traces show CER (B) and OER (C) in presence of 10 mM HBr. Dashed traces are similar experiments in solutions free of $Br^-$. Green, solid trace in C shows OER measured in 0.5 M $HClO_4$ and 10 mM HBr only (no $Cl^-$). Green, dashed trace in C shows 'pure OER', measured in 0.5 M $HClO_4$ (no $Cl^-$ and $Br^-$).*

Figure 5.5 shows the fitted and calculated individual current densities for the BER, CER and OER according to the above procedure. As previously established, the BER is suppressed by $Cl^-$, illustrated by negative values for $\mathcal{R}_{Cl^-}$. The CER is mutually strongly inhibited by $Br^-$, which shifts the onset potential for the CER around 50 mV more positive (Figure 5.5B). The OER is also negatively affected by $Br^-$ (thick, green traces in Figure 5.5C), and $Cl^-$ further decreases the activity, showing that $Br^-$ and $Cl^-$ suppress the OER in an additive way. During measurements in 10 mM HBr and 100 mM HCl, the OER activity can become almost immeasurably small (Figure 5.5C). At the same time, we observed that all measurable OER Tafel slopes are roughly similar, implying that the mechanism does not change under the effect of either $Br^-$ and $Cl^-$ (Figure A 9.5.14B). The retardation of the reaction is therefore probably caused by active site blocking.

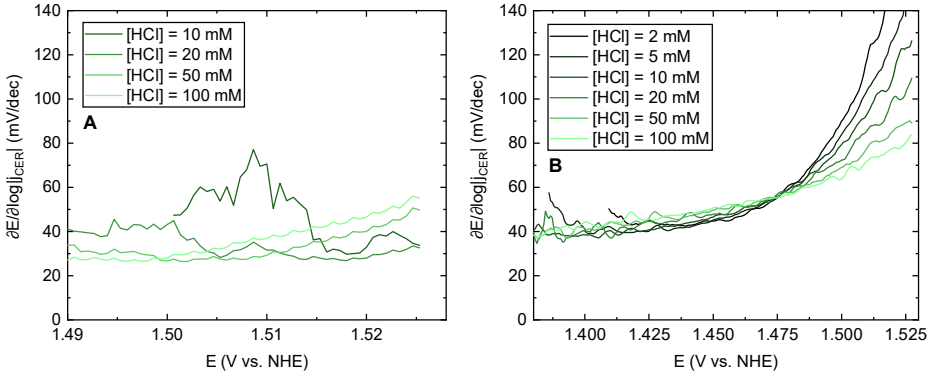


*Figure 5.6: CER Tafel slopes, measured in presence (A) and absence (B) of 10 mM HBr, based on data from Figure 5.5. Data for chloride concentrations lower than 10 mM in A had insufficient signal to noise ratio and were omitted.*

From the partial current densities in Figure 5.5, it is possible to determine Tafel slopes for the CER, as well as values of $\mathcal{R}_{Cl^-}$ in presence and absence of $Br^-$, as shown in Figure 5.6 and Figure 5.7. In Figure 5.6B, Tafel slopes for the CER competing with the OER generally start close to 40 mV/dec and then steadily increase. It is interesting to note that measurements in low [HCl] (such as 2 mM) show a sharp rise of slope beyond 120 mV/dec, like the BER did in section 5.3.3. The reason is probably the onset of diffusion limitations, as the rates measured at the high potential limit were within 40-50% of the Levich limiting current density for the 2 – 5 mM experiments. At chloride concentrations higher than 5 mM, the Levich limiting current density was approached less closely. Diffusion control thus becomes less of a factor, implying that the reaction kinetics are slowed down as a result of the increasing $[Cl^-]$.

When comparing Figure 5.6B to data in Figure 5.6A, the upward curvature in the high potential limits disappears in the presence of $Br^-$, as can be explained by the much lower overall reaction rates and thus the virtual absence of diffusion control (see Figure 5.5B). Linear Tafel slopes in Figure 5.6A start around 30 mV/dec, within 1.49 - 150 V vs. NHE, which is slightly lower than 40 mV/dec. These values seemingly agree with predictions by the Volmer-Tafel mechanism, but are more likely related to errors in the model describing the underlying BER limiting current density, which possibly approaches the real limiting value too quickly.

Figure 5.7 shows $\mathcal{R}_{Cl^-}$ values for the CER and the effect of $Br^-$ (see Figure A 9.5.15). $Br^-$ strongly lowers the activity of the CER, while at the same time, reaction orders are higher when comparing Figure 5.7A and B, where in the latter, values are usually below 1. All values decrease with increasing $[Cl^-]$. Higher reaction orders can be expected when competitive adsorption by $Br^-$ decreases the chloride surface coverage $\theta_{Cl}$. A lower value of $\theta_{Cl}$ at the onset of the reaction means its contribution to the measured reaction order is higher (see the SI of Chapter 4, in section 9.4.2). The range of values spanned by $\mathcal{R}_{Cl^-}$ in Figure 5.7A is mostly within 1-2, agreeing with the V-H mechanism. Only the value at the highest $[Cl^-]$ is around 0.8, which falls outside of this range. Corresponding Tafel data for $[Cl^-] = 50$ mM and 100 mM in Figure 5.6A, which are the most accurate, are lower than in Figure 5.6B, but display roughly the same rate of change over the measured potential window. This suggests that like the BER,

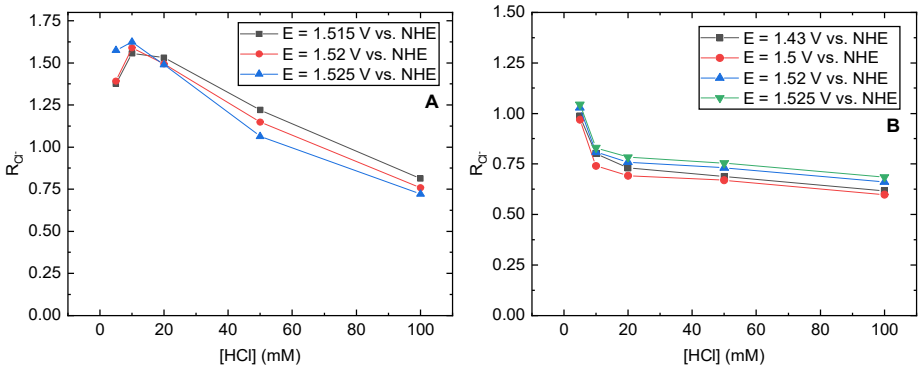


*Figure 5.7: Chloride reaction orders $\mathcal{R}_{Cl^-}$ for the CER, in presence (A) and absence (B) of 10 mM HBr, based on data from Figure 5.5. Potentials were chosen to span the range where significant CER occurs, which is much narrower for the CER in presence of $Br^-$. Data in B are only shown for $[Cl^-]$ values where the ring collection method is reliable (see section 2.3.3).*

the Tafel slopes as a whole are shifted horizontally on the potential axis. Together with the rising Tafel slopes as function of potential, this may be a coverage effect by $Cl^*$ when considering V-H or V-K as the dominant mechanism. We further analyzed the CER using Conway-Novák and Ferro-de Battisti test plots, which clearly point towards a V-H or V-K type mechanism for the CER, including when the reaction is inhibited by $Br^-$ (Figure A 9.5.13). It must be noted that linearity in Ferro-de Battisti test plots does not discern between the V-H and V-K mechanism, as their functional $j$ vs. $E$ relationship is the same. Distinction is in principle possible by investigating values of the slopes and y-intersects, but we refrained from this because these quantities are extremely sensitive to the value of the equilibrium potential, and become further convoluted when competitive adsorption is involved. It is in any case most likely that the values for $\mathcal{R}_{Cl^-}$ in Figure 5.7A and B correspond to V-H or V-K mechanisms with a first-order dependence on $\theta_{Cl}$.

Finally, we note that the significant depressing effect of $Cl^-$ on the OER activity is in stark contrast with results from Chapter 2, where the same $IrO_x$/GC electrode was studied for the CER. In a 0.5 M $KHSO_4$ electrolyte, $Cl^-$ has only a negligible effect on the OER activity, and the reaction order for the CER approaches values slightly less than 1 (see Figure A 9.5.15). It is likely the presence of $HSO_4^-$ that negates the suppressive effect of $Cl^-$ on the OER and CER, because OER and CER activities in such electrolytes were significantly lower than in a solution of non-adsorbing $ClO_4^-$. This strengthens the idea that chloride effects on the CER and OER in the current study are related to specific adsorption of $Cl^-$. In presence of excess $HSO_4^-$, the surface is already heavily under the influence of a competitive adsorbate. Addition of $Cl^-$ would then have a much smaller effect on the activity, because the reaction order effect from competitive adsorption is already near saturation. These results show that specific adsorption by the supporting electrolyte can have a significant effect on the apparent kinetics of the reaction and should be kept in mind when investigating concentration-dependent quantities.

### *5.3.6. Molar selectivities*

Lastly, we consider the molar selectivities $\varepsilon$ of the BER, CER and OER as function of the various halogen anion concentrations, which can be derived from data in Figure 5.7. Like Eq. 2.3, they can be calculated for a given value of $E$ or $[Cl^-]$ via:

$$\varepsilon_{BER} = \frac{j_{BER}/_2}{j_{BER}/_2 + j_{CER}/_2 + j_{OER}/_4} \qquad \text{Eq. 5.3}$$

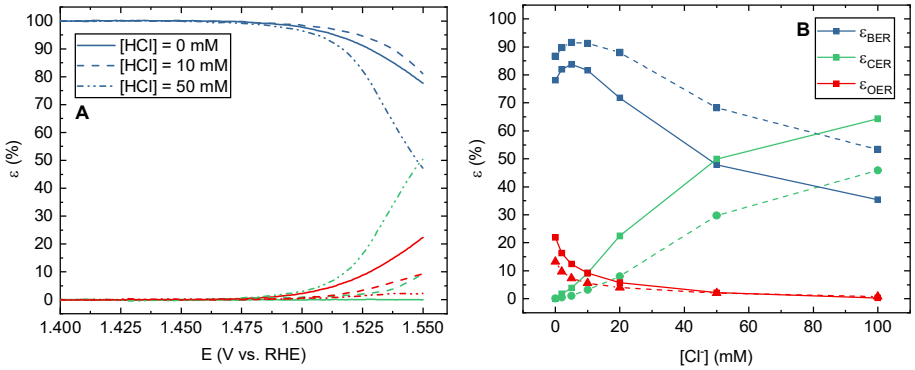


*Figure 5.8: Molar selectivities of the BER, CER, and OER in 0.5 M $HClO_4$ + 10 mM HBr. A: Data as function of potential, at chloride concentrations of 0 (solid trace), 10 (dashed trace) and 50 mM (dotted trace). Blue, green and red show selectivities for the BER, CER and OER, respectively. B: Data as function of chloride concentration at potentials of 1.535 (dashed trace) and 1.55 V vs. RHE (solid trace). These are potentials where all three reactions are prevalent.*

In Eq. 5.3, the BER selectivity is given as example. Figure 5.8 shows some measured selectivities of the three reactions. At lower potentials, the BER has near 100% selectivity, since it is the only possible reaction up until ~1.37 V. The CER has a significant overpotential due to the suppressive effect of $Br^-$, and onsets around the same potential as the OER. The BER is almost fully mass transport controlled at this point. Addition of $Cl^-$ has a two-fold effect on $\varepsilon_{BER}$, which decreases due to CER activity, but also increases due to suppression of the OER by $Cl^-$. This is clearly visible in Figure 5.8B, where $Cl^-$ increases the BER selectivity up until 10 mM $Cl^-$, after which it is decreases again with increasing CER competition. Another peculiarity of kinetic interplay arises when inspecting the OER and CER selectivities relative to each other, and the effect of bromide. In Figure A 9.5.16, when the CER and OER are the only reactions, the OER selectivity always increases with higher potential. In presence of $Br^-$ however, the selectivity decreases. OER selectivity is always quite low (<22%), and sharply decreases when $Cl^-$ is added. Less than 1% $O_2$ is formed at 100 mM $Cl^-$. The OER is much less sensitive to mass transport effects in an aqueous electrolyte, and should therefore still become the dominant reaction at potentials above 1.55 V vs. RHE. However, the overpotential where this happens will be dependent on $Br^-$ and $Cl^-$ in dual fashion. Besides the parallel BER and CER contributions, which must be outpaced, $Br^-$ and $Cl^-$ additionally impart significant kinetic suppression on OER itself and make the reaction even more sluggish. It was not

possible to measure reliable data at potentials higher than 1.55 V vs. RHE, because the increasing OER rates lead to persistent $O_2$ bubbles on the RRDE tip which compromise the measurements (see Chapter 8). We expect that generally, the OER selectivity versus halogen oxidation will depend sensitively on the electrode material, mass transport conditions and electrolyte composition. Small reactant concentrations can already significantly affect the interplay between kinetics. The possible effects of $Br^-$ in the context of saline water electrolysis, even when present in small amounts, must thus not be underestimated.

## 5.4. Conclusions

In this chapter, we studied the simultaneous oxidation of $Br^-$, $Cl^-$ and $H_2O$ on GC-supported $IrO_x$, which served as a representative OER catalyst in practical electrolyzers. Adsorption and oxidation of $Br^-$ and $Cl^-$ proceeded simultaneously and had notable mutual effects on their respective evolution reactions. Bromine evolution exhibited reaction orders $\mathcal{R}_{Br^-}$ that are significantly higher than 1 at kinetically controlled potentials, but semi-linear Tafel slopes of 90-110 mV/dec. Chloride addition shifted the slopes to slightly higher values and was associated with mildly inhibiting effects ($\mathcal{R}_{Cl^-} \approx -0.1$). Together with the use of test plots, the Volmer-Heyrovský mechanism with a Langmuirian isotherm describing competitive adsorption of the halogen anions seems to describe the BER mechanism on $IrO_x$ the most adequately. The CER displays previously reported linear Tafel slopes of ~40 mV/dec, also in presence of $Br^-$. Chloride reaction orders had values $0.7 < \mathcal{R}_{Cl^-} < 1$, but under the effect of $Br^-$ they were significantly higher than 2. Together with test plots, the Volmer-Heyrovský again is the most suitable description for the experimental results. The lower limit values for chloride reaction orders which fall outside the predicted range of the V-H mechanism were ascribed to site-blocking (retardation of the CER by specific adsorption of chloride).

The OER was particularly slowed down by a compounded effect of both $Br^-$ and $Cl^-$. Similar to the effects observed for the CER, the nature of this effect seemed to be a type of 'simple' competitive adsorption through site blocking, as the Tafel slopes (and therefore the underlying mechanism) did not seem to change. The selectivity for the OER was close to 0 at 1.55 V vs. RHE in conditions of 10 mM HBr and 100 mM HCl, which were the maximum concentrations tested. Contrary to findings on Pt in Chapter 4, no signs of BrCl formation were observed, even though $Br^-$ and $Cl^-$ interact strongly during adsorption. Kinetic analysis of the bromide oxidation region and UV-Vis experiments suggested that the only electrochemically formed products are $Br_2$, $Cl_2$ and $O_2$.